Local Spectral Analysis of Short-Pulse Excited Scattering from Weakly Inhomogeneous Media—Part II: Inverse Scattering

Timor Melamed, Ehud Heyman, *Senior Member, IEEE*, and Leopold B. Felsen, *Life Fellow, IEEE*

***Abstract*— This paper is concerned with the reconstruction of a weakly inhomogeneous scattering profile from data generated by a short-pulse incident plane wave, which is postprocessed so as to localize the interrogated region to a space–time resolved scattering cell. The phase-space localization due to postprocessing is brought about by applying local (i.e., windowed) slant-stack transforms to the time-dependent scattered fields. In the domain of the scatterer, this processing corresponds to applying windowed Radon transforms to the induced field distribution, which, in turn, generates pulsed-beam (PB) wave packets traveling *toward* the observer. The forward analysis parameterizing this new form of time-domain (TD) diffraction tomography has been performed in a companion paper and furnishes the framework for the investigation here. Via the forward parameterization, the three-dimensional (3-D) global scattering phenomenology has been reduced to scattering from an equivalent one-dimensional (1-D) scattering cell oriented along the bisector between the direction of the incident plane pulse and the direction of the scattered pulsed beam (PB) to the observer. For the inverse problem, this process is reversed by windowing the scattered field and backpropagating the resulting PB's so as to form local images of any selected region in the scattering domain. The phase-space signature of the scattering cell is related to the Radon transform of the medium in the cell so that the local profile function can be recovered by Radon inversion. An illustrative numerical example is included. Also discussed is the ultimate localization achieved by incident PB excitation *and* PB postprocessing of the scattered field.**

***Index Terms*— Electromagnetic scattering, inverse problems, nonhomogeneous media, pulsed beams.**

I. Introduction

In this second part of the two-part presentation, we deal with the reconstruction of a pulsed-plane-wave excited Born-approximated scattering object $O(\mathbf{r})$ in [1, fig. I] by inversion of locally windowed (postprocessed) scattered field data observed on the measurement planes z_j, $j = 1, 2$, within which the object is located.

The windowed postprocessing provides the initial conditions for backpropagation of localized pulsed-beam (PB) wave objects toward the object domain. Part I of this study treats the direct (forward) scattering problem in which $O(\mathbf{r})$ is assumed to be specified and the Born-approximated time-dependent induced sources in the pulsed plane wave illuminated $\mathbf{r}$ domain are known. These induced sources, when subjected to space–time windowed transforms, radiate a highly localized phase-space PB that can be steered to any space–time point $(\mathbf{x}, t)_{z_j}$ on the measurement planes z_j. The induced scattering cell, which generates the scattered PB, is an equivalent one-dimensionally (1-D) stratified region oriented along the bisector between the direction of incidence and observation [1] (also see [2]). When applying the PB parameterization for the forward problem to the profile inversion, the space–time windowed portions of the $(\mathbf{x}, t)_{z_j}$ data are "back propagated" as phase-space PB's toward the object domain $O(\mathbf{r})$. The PB backpropagated data contains the phase-space footprints of that localized region around a point $\mathbf{r}_o$ in $O(\mathbf{r})$, sampled at time t_o, which *established* the $(\mathbf{x}, t)$ data on z_j. The $(\mathbf{r}_o, t_o)$ phase-space footprints are now processed so as to extract from them the *explicit* physical profile $O(\mathbf{r})$ in the vicinity of $\mathbf{r}_o$. In view of the results of Part I, this reconstruction strategy yields the local profile along the $\mathbf{s}_j$ bisector in [1, fig. 6].

This brief and qualitative description of the inversion process is formalized in the body of this paper by detailed analysis and synthesis. Most of the necessary operations shall be performed directly in the time domain (TD). Whenever desired, the frequency-domain analog of the inversion process here can be inferred from the corresponding frequency-domain forward processing in Part I, where the time and frequency domains are treated side by side. In the text that follows, backpropagation as such is considered in Section II-A, while in Section II-B, we discuss localized (windowed) spectra, summarizing in Section II-B1 the relevant forward results from [1], which are then transformed in Sections II-B2 and II-B3 into their backpropagated analogs. Special attention is given to the TD Gaussian δ windows which generate the PB's. Object reconstruction, using the phase-space footprints in Section II, is performed in Section III. After providing the formally exact (but very massive) global phase-space inversion algorithms, emphasis is placed (in Section IV) on the substantial simplifications, which result due to the space-

Manuscript received September 3, 1997; revised January 5, 1998. This work was supported in part by the U.S.–Israel Binational Science Foundation, Jerusalem, Israel, under Grants 92-00273 and 95-00399. The work of T. Melamed was supported by a 1996–1997 Dean's Postdoctoral Fellowship, Boston University. The work of E. Heyman was supported in part by the U.S. Air Force Office of Scientific Research under Grant 96-1-0039. The work of L. B. Felsen was supported in part by the Naval Coastal Systems Center, Panama City, FL, under ONR Grant N61331-96-K-0028.

T. Melamed and E. Heyman are with the Department of Electrical Engineering, Physical Electronics, Tel-Aviv University, Tel-Aviv, 69978 Israel.

L. B. Felsen is with the Department of Aerospace and Mechanical Engineering and the Department of Electrical and Computer Engineering, Boston University, Boston, MA 02215 USA.

Publisher Item Identifier S 0018-926X(99)05816-0.

time localization of PB processing and use of asymptotic techniques. Numerical examples implementing the forward algorithms in [1] and the inverse algorithms in the present paper are discussed in Section V, with attention paid to the sensitivity of the results with respect the pulse and processing window parameters. Conclusions are presented in Section VI.

The pulsed plane wave input employed in this study sets the stage for an implementation of the "ultimate" localization wherein the incident field is preprocessed via localized phase-space windowing so as to generate a PB input, and the scattered field is postprocessed so as to generate a PB output. This ultimate *a priori* localization favors modeling of the scattering process in terms of Fermat ray paths from the $(\mathbf{x}, t)$ launch points on z_j (via the object domain) to the observer on z_j, with the scattering strength determined by the $O(\mathbf{r}_o)$ profile sampled at time t_o along the bisector $\mathbf{s}_j$ between the incident PB direction and the direction of scattering $\overline{\boldsymbol{\xi}}$ toward $(\mathbf{x}, t)_{z_j}$. This process is schematized in Fig. 9 and it is quantified for the forward and inverse scenarios as part of the conclusions in Section VI.

II. Phase-Space Backpropagation

A. Time-Dependent Plane Wave Representation

The spectral characteristics that distinguish backpropagation from forward propagation are demonstrated most directly for plane waves. We shall retain the notation used in Part I, which makes the formulation directly applicable to the *scattering* configuration depicted in [1, fig. I]. Since the scatterer is located *between* the "data" planes z_1 and z_2, scattering toward z_1 takes place along the negative z axis and toward z_2 along the positive z axis. Thus, *forward* propagation away from data planes z_1 and z_2 covers the regions $z < z_1$ and $z > z_2$, respectively, with corresponding upper and lower signs as shown in [1, eq. (10)] (here and elsewhere the subscript $j = 1, 2$ denotes constituents corresponding to data taken on the z_j plane). *Backpropagation*, defined by tracking the scattered field back to the source domain is, therefore, given by the same expressions as in [1, eq. (10)] but for $z \gtrless z_j$, respectively. In Part I, [1, eq. (10)] is written directly in the TD as an angular superposition of time-dependent plane waves [or pulsed plane waves (PPW)]. Here $\tilde{u}_j(\overline{\boldsymbol{\xi}}, \tau)$ is the TD plane wave spectrum, calculated from the data field $u_j(\mathbf{x}, t)$ by the slant stack transform (SST) in [1, eq. (8)] with $\boldsymbol{\xi} = (\xi_1, \xi_2)$ and $\zeta \equiv \sqrt{1 - \boldsymbol{\xi} \cdot \boldsymbol{\xi}}$, $\operatorname{Im} \zeta \geq 0$ being the normalized transverse and longitudinal wavenumbers, respectively.

In Part I, [1, eq. (10)] incorporates only the contribution of the propagating spectrum $|\boldsymbol{\xi}| < 1$ wherein ζ is real. Extending to account for the contribution of the evanescent spectrum $|\boldsymbol{\xi}| > 1$, wherein $\zeta = i|\zeta|$, can be implemented by utilizing analytic signals that accommodate the complex time delay implied by imaginary ζ [3]. The *total* analytic field $\overset{+}{u}_j$ is thus given by the right-hand side of [1, eq. (10)] wherein $\tilde{u}_j$ is replaced by its analytic counterpart $\overset{+}{\tilde{u}}_j$ and the integration domain now extends over the entire $\overline{\boldsymbol{\xi}}$ plane (the real field is given by the real part of $\overset{+}{u}_j$). One finds that the evanescent spectrum contribution decays when *forward*-propagated away from the initial plane, but grows when *backpropagated* toward the object domain. In order to avoid numerical amplification of measurement errors or noise, the backpropagated fields $u_j^b(\mathbf{r}, t)$ are defined only with respect to the propagating spectrum, i.e., by [1, eq. (10)] extended to the range $z \gtrless z_j$. These rules apply to all conversions of forward propagated TD spectra in [1] into the backpropagated spectra required here.

B. Local Spectrum Analysis and Pulsed-Beam Backpropagation

Local spectral analysis of a given space–time-dependent field distribution is effected by application of windowed SST. We summarize first the relevant results from the forward analysis in [1, sec. III-B2] and [1, sec. III-B3] and proceed then to backpropagation.

1) Transform Relations: The time-dependent local spectrum of the field data $u_j(\mathbf{x}, t)$ on the z_j planes of [1, fig. I] is defined by [1, eq. (14)]

$$U_j(\mathbf{Y}) = \int d^2x \int dt u_j(\mathbf{x}, t) W(\mathbf{x}, t; \mathbf{Y}) \qquad \mathbf{Y} \equiv (\mathbf{X}, \overline{t}),\ \mathbf{X} \equiv (\overline{\mathbf{x}}, \overline{\boldsymbol{\xi}}) \tag{1}$$

with W being a space–time window [1, eq. (15)]. The space–time and spectral dependence in W imply that the window is localized in the $(\mathbf{x}, t)$ data plane about $(\overline{\mathbf{x}}, \overline{t})$, with spectral tilt $\overline{\boldsymbol{\xi}}$ (see [1, fig. 4]). The operation in (1) has, therefore, been referred to in [1] as a "*local slant stack transform*" that extracts the local spectral information from the time dependent data. Thus, $U_j(\mathbf{Y})$ is localized *a priori* around a time $\overline{t}(\overline{\mathbf{x}})$ and wave-tilt $\overline{\boldsymbol{\xi}}(\overline{\mathbf{x}})$ that describe the arrival time and direction of the scattered field at that point.

2) Pulsed-Beam Propagation: The scattered fields $u_j(\mathbf{r}, t)$ in the regions $z \lessgtr z_j$ can be expressed by propagating $u_j(\mathbf{x}, t)$ away from the data planes. This forward propagation into the regions $z \lessgtr z_j$ is obtained by replacing the window functions $W_N(\mathbf{x}, t; \mathbf{Y})$ in the local representation [1, eq. (16)] by the phase-space propagators $B_j(\mathbf{r}, t; \mathbf{Y})$, i.e., [4, eq. (44)]

$$u_j(\mathbf{r}, t) = -(2\pi v_o)^{-2} \int d^5 Y U_j(\mathbf{Y}) B_j(\mathbf{r}, t; \mathbf{Y}). \tag{2}$$

To synthesize $B_j(\mathbf{r}, t; \mathbf{Y})$ from its initial field distribution $W_N(\mathbf{x}, t; \mathbf{Y})$ on the z_j plane, we use the transient plane wave representation in [1, eq. (10)], but in order to accommodate both the propagating and the evanescent spectra we employ the analytic signal extension, i.e., $B_j(\mathbf{r}, t; \mathbf{Y}) = \operatorname{Re} \overset{+}{B}_j(\mathbf{r}, t; \mathbf{Y})$ with (see [4, eq. (46)])

$$\overset{+}{B}_j(\mathbf{r}, t; \mathbf{Y}) = -(2\pi v_o)^{-2} \int d^2\xi\, \partial_t^2 \overset{+}{W}_N(\boldsymbol{\xi}, t - v_o^{-1}(\boldsymbol{\xi} \cdot \mathbf{x} \mp \zeta(z - z_j)); \mathbf{Y}) z \lessgtr z_j \tag{3}$$

where $\overset{+}{\tilde{W}}_N(\boldsymbol{\xi}, \tau; \mathbf{Y})$ is the analytic SST of W_N, calculated via the analytic signal extension of [1, eq. (8)]. For W_N of [1, eq. (16)], it is given by

$$\overset{+}{\tilde{W}}_N(\boldsymbol{\xi}, \tau; \mathbf{Y}) = N^{\dagger}(\tau) \overset{\tau}{\otimes} \overset{+}{\tilde{w}}(\boldsymbol{\xi} - \overline{\boldsymbol{\xi}}, \tau - \overline{t} + v_o^{-1} \boldsymbol{\xi} \cdot \overline{\mathbf{x}}) \tag{4}$$

and $\overset{+}{\tilde{w}}(\boldsymbol{\xi}, \tau)$ denotes SST of $w(\mathbf{x}, t)$. Since $W_N(\mathbf{x}, \boldsymbol{\xi}, t)$ is localized about $(\overline{\mathbf{x}}, \overline{\boldsymbol{\xi}}, \overline{t})$, B_j is a space–time wavepacket, a PB that emerges from the z_j plane at $(\mathbf{x}, t) = (\overline{\mathbf{x}}, \overline{t})$ in the direction $\mathring{\overline{\kappa}}_j = (\overline{\boldsymbol{\xi}}, \mp\overline{\zeta})$ where $\overline{\zeta} = \sqrt{1 - \overline{\boldsymbol{\xi}} \cdot \overline{\boldsymbol{\xi}}}$ [1, eq. (17), fig. 1]. An asymptotically approximated explicit form for B_j is given in (8) below.

For properly chosen window parameters, the PB's remain collimated and well localized about the *observation constraint* defined in [1, eq. (18)]. For a given phase-space point $\mathbf{Y} = (\overline{\mathbf{x}}, \overline{\boldsymbol{\xi}}, \overline{t})$, this constraint defines the space–time trajectory of the PB, which emerges from $(\overline{\mathbf{x}}, \overline{t})$ on the data planes z_j with spectral direction $\overline{\boldsymbol{\xi}}$. Alternatively, for a given space-time observation point $(\mathbf{r}, t)$, [1, eq. (18)] defines the center coordinates $\mathbf{Y}(\mathbf{r}, t)$ of the phase-space region that contributes significantly at $(\mathbf{r}, t)$. Further localization of the phase-space integral (2) is due to the fact that the local spectrum $U_j(\mathbf{Y})$ of the data is localized as discussed after [1, eq. (17)].

3) Pulsed-Beam Backpropagation: Referring to Section II-A, we construct the backpropagated counterpart of (2) by extending the definition of $\overset{+}{B}$ in (3) to the range $z \gtrless z_j$, respectively, i.e.,

$$u_j^b(\mathbf{r}, t) = -(2\pi v_o)^{-2} \int d^5 Y U_j(\mathbf{Y}) B_j^b(\mathbf{r}, t; \mathbf{Y}). \quad (5)$$

This expression is similar to (2) except that the backpropagators B_j^b are now obtained by extending the definition of B_j in (3) to the range $z \gtrless z_j$; recalling the discussion in Section II-A, the spectral integration range in (3) is now restricted to $|\boldsymbol{\xi}| < 1$. The formal representation in (5) may be further simplified if we note from (4) that the kernel $\overset{+}{W}_N$ in (3) is localized about $\boldsymbol{\xi} = \overline{\boldsymbol{\xi}}$, so that only PB's with $|\overline{\boldsymbol{\xi}}| < 1$ are significantly excited by (3). Consequently, the phase-space integration in (5) becomes

$$u_j^b(\mathbf{r}, t) = -(2\pi v_o)^{-2} \int_{|\overline{\boldsymbol{\xi}}|<1} d^5 Y U_j(\mathbf{Y}) B_j^b(\mathbf{r}, t; \mathbf{Y}). \quad (6)$$

Equation (5) [or (6)] expresses the backpropagated fields $u_j^b(\mathbf{r}, t)$ as a superposition of backpropagated PB's weighted by the local spectrum $U_j(\mathbf{Y})$ and emanating from the data planes in all directions toward the object domain. As discussed after [1, eq. (16)], the phase-space data $U_j(\mathbf{Y})$ is localized and thus the integration domain in (2) may be limited *a priori* to the relevant phase-space regions. Further localization is effected by the PB backpropagators via the *observation constraint*, which, for a given observation point $(\mathbf{r}, t)$ in the object domain, becomes (cf. [1, eq. (18)]; noe the different sign in $\overline{t}$)

$$\frac{\mathbf{x} - \overline{\mathbf{x}}}{\mp(z - z_j)} = \frac{\overline{\boldsymbol{\xi}}}{\overline{\zeta}}, \qquad \overline{t} = t + v_o^{-1} \sqrt{|\mathbf{x} - \overline{\mathbf{x}}|^2 + (z - z_j)^2}. \quad (7)$$

This constraint is used in Section III-B to further simplify the phase-space integration in (5).

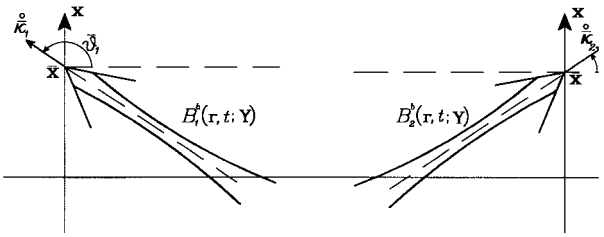

Fig. 1. Backpropagated beams.

4) Special Case: Gaussian δ Windows: Closed-form expressions for the backpropagated PB's can be found for the class of TD Gaussian δ windows [1, eq. (38)] discussed in [1, sec. IV-E]. This window is localized around $(\mathbf{x}, t) = (0, 0)$. Its properties and the role of the parameters β and T have been discussed in [1, eqs. (37)–(43)]. Note that the window is multiplied by a complex parameter α whose role will become apparent in (23) in connection with the imaging algorithm.

Near the beam axis, the spectral integral in (3) can be evaluated asymptotically via the procedure in [4, Appendix], which consists of transformation to the beam coordinates followed by saddle-point integration of the Fourier inversion to the TD. The resulting *forward* paraxial propagators for $z \lessgtr z_j$ are given in [4, eq. (69)]. In view of the discussion above, the paraxial *backpropagators* B_j^b are given by the same expressions extended to the region $z \gtrless z_j$, i.e.,

$$B_j^b(\mathbf{r}, t; \mathbf{Y}) \sim \mathrm{Re}\, \frac{i\alpha\beta_r}{\pi v_o |\beta|^2} \sqrt{\frac{\det \mathbf{Q}_j^b(z_{b_j})}{\det \mathbf{Q}_j^b(0)}} \overset{+}{\delta}{}^{(1)}\left[t - \overline{t} - \frac{i}{2} T - v_o^{-1}\left(z_{b_j} + \frac{1}{2} \mathbf{x}_{b_j} \cdot \mathbf{Q}_j^b(z_{b_j}) \cdot \mathbf{x}_{b_j}\right)\right]. \quad (8)$$

with (contrast [1, eq. (45)])

$$\mathbf{Q}_j^b(z_{b_j}) = \begin{bmatrix} (z_{b_j} - i\beta\overline{\zeta}^2)^{-1} & 0 \\ 0 & (z_{b_j} - i\beta)^{-1} \end{bmatrix}. \quad (9)$$

Referring to Figs. 1 and [1, fig. 7], the beam coordinates $\mathbf{r}_{b_j} = (x_{b_{1j}}, x_{b_{2j}}, z_{b_j})$ are defined for a given phase-space point $\mathbf{Y}$ by the transformation in [1, eq. (46)]. Thus, (8) represents *forward* propagation for $z_{b_j} > 0$ and *backpropagation* for $z_{b_j} < 0$. Following the same analysis as in [4] (see also [1, eqs. (48)–(52)]), we find that the PB in (8) is astigmatic with major axes along the $x_{b_{lj}}$ directions $l = 1, 2$; its *waist* in the $(z_{b_j}, x_{b_{lj}})$ plane is located at $z_{b_j} = Z_l$, with *collimation length* F_l, where Z_l and F_l are defined in [1, eq. (49)].

III. Object Reconstruction

A. Inversion Strategy

As outlined qualitatively in Section I, localized object reconstruction from the scattered field data $u_j(\mathbf{x}, t)$ on the z_j planes is based on backpropagation of the "footprint" in the data. In the local analysis approach, the footprints $U_j(\mathbf{Y})$ are extracted from the data in (1) via the time-dependent window W and are transported toward the object domain by

the PB backpropagators B_j^b so as to synthesize via (6) the backpropagated field $u_j^b(\mathbf{r}, t)$. As has been shown in [1] and [2], the local spectra $U_j(\mathbf{Y})$ are also related to local samples of the object function $O(\mathbf{r})$ via [1, eq. (26)]; thus, the local samples can be recovered from $U_j(\mathbf{Y})$ by deconvolution and inversion.

The relation between the backpropagated fields and the reconstructed object function has been established in [5]: $O(\mathbf{r})$ is a sum of two terms $O(\mathbf{r}) = O_1(\mathbf{r}) + O_2(\mathbf{r})$, where $O_j(\mathbf{r})$, $j = 1, 2$ are the partial images reconstructed by the backpropagated fields u_j^b from the z_j planes

$$O_j(\mathbf{r}) = 2v_o^{-1}\partial_z\{f^\dagger(t + v_o^{-1}z) \overset{t}{\otimes} u_j^I(\mathbf{r}, t)\}|_{t=0} \tag{10}$$

with u_j^I related to the backpropagated fields u_j^b via

$$u_j^I(\mathbf{r}, t) = -v_o^2\partial_t^{-2}u_j^b(\mathbf{r}, t). \tag{11}$$

The convolution in (10) with

$$f^\dagger(t) \equiv \frac{1}{2\pi}\int_{|\omega|<\omega_{max}} d\omega e^{-i\omega t}[\hat{f}(\omega)]^{-1} \tag{12}$$

deconvolves the exciting signal $f(t)$ from the data, $\omega_{\max}$ being the upper frequency considered. If $f(t)$ is short with respect to the scale of the object and $\hat{f}(\omega) \simeq 1$ for $\omega < \omega_{\max}$, then $f(t) \simeq \delta(t)$ and (10) may be simplified to

$$O_j(\mathbf{r}) \simeq 2v_o^{-1}\partial_z u_j^I(\mathbf{r}, t)|_{t=z/v_o}. \tag{13}$$

Further particulars in implementing the inversion sequence are given below.

1) The window $w(\mathbf{x}, t)$ in (1) is the twice-differentiated Gaussian δ window in [1, eq. (38)]. This window contains three parameters: T; α; and β. T is chosen to be of the same order as (or smaller than) the exciting pulse length. The choice of the factor α depends on the processing scheme [see (23)]. For β we may consider two options:
   a) $\beta = \beta_r > 0$ pure real with β_r being of the same order as the distance from the data plane to the object (image) domain; the resulting PB backpropagator will have its waist at the data plane while the object domain will still be in the collimation (Fresnel) zone [1, eq. (49)];
   b) $\beta = \beta_r + i\beta_i$, with β_r defined as in option a) while $\beta_i \simeq \beta_r$; this yields a converging PB backpropagator that has its waist in the image domain, while the data plane will still be in the collimation zone [1, eq. (49)].
2) When calculating the backpropagated field in (6), only those PB's whose beam axes pass near $\mathbf{r}$ contribute. These beams satisfy the "observation constraint" in (7). Consequently, only those phase-space regions near the observation constraint contribute to the integration.
3) In view of the restrictions in 2), the PB backpropagators are approximated by their explicit asymptotic forms in (8).

The inherent localizations enumerated above simplify the formal inversion steps substantially.

B. Implementation via Constrained Evaluation

Since the phase-space backpropagation integral (6) for $u_j^b(\mathbf{r}, t)$ is localized about the vicinity of the observation constraint (7), one may try to evaluate part of this integral analytically, thereby reducing the computational complexity. We shall briefly present such a scheme, referring for details to [6, sec. 6.2].

In view of the "imaging condition" $t = z/v_o$ in (13), the integral (6) can be localized about the observation constraint (7) with $t \to z/v_o$. For a given object point $\mathbf{r}$, this constraint defines $\overline{\boldsymbol{\xi}} = \overline{\boldsymbol{\xi}}(\overline{\mathbf{x}})$ and $\overline{t} = \overline{t}(\overline{\mathbf{x}})$ as functions of $\overline{\mathbf{x}}$. Noting that the local spectrum $U_j(\mathbf{Y})$ is due to volume scattering [1, eq. (26)] and is thus typically less localized than $B_j^b(\mathbf{r}, t; \mathbf{Y})$, it may be approximated in (5) by the constrained value $U_j(\overline{\mathbf{x}}, \overline{\boldsymbol{\xi}}(\overline{\mathbf{x}}), \overline{t}) \equiv U_j^C(\overline{\mathbf{x}}, \overline{t})$ where the superscript "C" identifies data associated with the constraint relation. Combining (2) with (11) we obtain

$$u_j^I(\mathbf{r}, t) \approx (2\pi)^{-2}\int d^2\overline{x}\int d\overline{t} U_j^C(\overline{\mathbf{x}}, \overline{t})\mathcal{G}_j^b(\mathbf{r}, t; \overline{\mathbf{x}}, \overline{t}) \tag{14}$$

where the propagator

$$\mathcal{G}_j^b(\mathbf{r}, t; \overline{\mathbf{x}}, \overline{t}) = \int d^2\overline{\xi}\partial_t^{-2}B_j^b(\mathbf{r}, t; \mathbf{Y}) \tag{15}$$

accounts for the $\overline{\xi}$ integration in (2). Expressing $B_j^b(\mathbf{r}, t; \mathbf{Y})$ by its plane wave spectrum representation (3) and inverting the order of integrations, one may obtain a closed-form expression for $\mathcal{G}_j^b$ (see [6, sec. 6.2]).

IV. Processing and Inversion Along the Beam Axes

A. Forward Modeling

In this section, we utilize the local (phase-space) TD diffraction tomography relation in [1, eq. (26)], in which the local spectrum of the data is related to a local sample of $O(\mathbf{r})$ along the PB axis, to derive an approximate closed-form inversion formula along this axis. The *forward* problem has been analyzed in [1, sec. IV-C] and interpreted there as follows: the local spectrum of the scattered field around the space-time point $(\overline{\mathbf{x}}, \overline{t})$ on the z_j plane corresponds to a local Radon transform of $O(\mathbf{r})$ at points $\mathbf{r}_o(\mathbf{Y})$ on the beam axis corresponding to $\mathbf{X} = (\overline{\mathbf{x}}, \overline{\boldsymbol{\xi}})$ [1, eq. (28), fig. 6]. The local Radon transform is taken in the direction $\overset{\circ}{\mathbf{s}}_j$ defined in [1, eq. (32)] and [1, eq. (33)] that bisects the angle between the direction of incidence of the PPW and the direction of observation $\overset{\circ}{\boldsymbol{\kappa}}_j$ along the beam axis [1, fig. 6)].

If the window width in the local Radon transform is small with respect to the transverse variations of $O(\mathbf{r})$, the scattering process generating the local spectrum can be viewed as local reflections from an equivalent plane stratified medium whose axis of stratification is along $\overset{\circ}{\mathbf{s}}_j$. Thus, for a given $\mathbf{X}$, $U_j(\mathbf{Y})$ is a function of $\overline{t}$ that describes PB reflections by an equivalent plane stratified medium along the beam axis corresponding to $\mathbf{X}$.

Referring to Fig. 2, scattering-window-based coordinates $\mathbf{r}_{s_j} = (x_{s_{1j}}, x_{s_{2j}}, s)$ are introduced with origin at the center

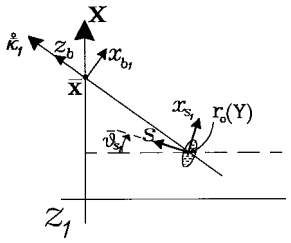

Fig. 2. $\mathbf{r}_{s_j}$ coordinate system: centered at $\mathbf{r}_o(\mathbf{Y})$ and oriented along the window normal $\hat{\mathbf{s}}_j$.

$\mathbf{r}_o(\mathbf{Y})$ of the sampling window $\Lambda_j(\mathbf{r}, \mathbf{Y})$ (see [1, eqs. (28), (33)])

$$\mathbf{r}_o(\mathbf{Y}) = (\bar{\mathbf{x}}, z_j) + z_{b_j}\hat{\bar{\boldsymbol{\kappa}}}_j, \quad z_{b_j} = -(v_o\bar{t} - z_j)/2\cos^2\bar{\vartheta}_{s_j}. \tag{16}$$

The window plane $(x_{s_{1j}}, x_{s_{2j}})$ is perpendicular to the direction of the normal $\hat{\mathbf{s}}_j$ (see Fig. 2). The $\mathbf{r}_{s_j}$ coordinates are obtained from the beam coordinates $\mathbf{r}_{b_j} = (x_{b_{1j}}, x_{b_{2j}}, z_{b_j})$ used in (8) by rotation in the $(z_{b_j}, x_{b_{1j}})$ plane through the bisector angle $\bar{\vartheta}_{s_j}$ in [1, eq. (33)]. Using the z_{b_j} coordinate of the window center in (16) we obtain

$$\begin{bmatrix} x_{s_{1j}} \\ s \end{bmatrix} = \begin{bmatrix} \cos\bar{\vartheta}_{s_j} & \pm\sin\bar{\vartheta}_{s_j} \\ \mp\sin\bar{\vartheta}_{s_j} & \cos\bar{\vartheta}_{s_j} \end{bmatrix} \begin{bmatrix} x_{b_{1j}} \\ z_{b_j} + \dfrac{v_o\bar{t} - z_j}{2\cos^2\bar{\vartheta}_{s_j}} \end{bmatrix}$$
$$x_{s_{2j}} = x_{b_{2j}}. \tag{17}$$

The phenomenology and parameterization of the forward scattering problem will now be utilized for the *inverse* problem of identifying the profile of the equivalent 1-D plane stratified medium along the axis of the phase-space-processed backpropagated PB from the scattered field data on the z_j planes to the object domain $O(\mathbf{r})$. Assuming that $O(\mathbf{r})$ is approximately constant over the window width transverse to the s axis, the local Radon transform operation in [1, eq. (26)] can be approximated by

$$U_j(\mathbf{Y}) \simeq f(\bar{t}) \overset{\bar{t}}{\otimes} \int ds O_c(s; \mathbf{Y})\Gamma_j(s; \mathbf{Y}) \tag{18}$$

where $O_c(s; \mathbf{Y})$ is the value of $O(\mathbf{r})$ along the $\hat{\mathbf{s}}_j$ axis corresponding to $\mathbf{Y}$, with $s = 0$ defining the window center at $\mathbf{r}_o(\mathbf{Y})$. In (18) the kernel

$$\Gamma_j(s; \mathbf{Y}) = \int dx_{1j} \int dx_{2j} \Lambda_j(\mathbf{r}; \mathbf{Y}) \tag{19}$$

incorporates, through the $\mathbf{x}_{s_j}$ integration, the effect of the "domain of influence" of the window Λ_j in planes transverse to $\hat{\mathbf{s}}_j$. As will be shown below $\Gamma_j(s; \mathbf{Y})$ is a 1-D window kernel that samples $O_c(s; \mathbf{Y})$ about $s = 0$ [i.e., about $\mathbf{r}_o(\mathbf{Y})$].

B. Gaussian Windows

A simple closed-form asymptotic expression for Γ_j and for the related operations in (18) may be obtained for the time-dependent Gaussian δ window in [1, eq. (38)], which has been used throughout this investigation. The approximate sampling window $\Lambda_j(\mathbf{r}; \mathbf{Y})$ corresponding to this window is given in [1, eq. (56)]

$$\Lambda_j(\mathbf{r}; \mathbf{Y}) \sim \mathrm{Re}\,\frac{-\alpha^*}{2v_o\bar{\zeta}}\sqrt{\frac{\det\mathbf{Q}_j(z_b)}{\det\mathbf{Q}_j(0)}} \overset{+}{\delta}{}^{(3)}\left[\bar{t} - \frac{i}{2}T - v_o^{-1}\left(z - z_{b_j} + \frac{1}{2}\mathbf{x}_{b_j}\cdot\mathbf{Q}_j\cdot\mathbf{x}_{b_j}\right)\right]. \tag{20}$$

Using the window-centered coordinates in (17) as well as the beam axis coordinates in [1, eq. (46)], we identify $z - z_{b_j} = v_o\bar{t} - 2s\cos\bar{\vartheta}_{s_j}$, $x_{b_{1j}} = x_{s_{1j}}\cos\bar{\vartheta}_{s_j} \mp s\sin\bar{\vartheta}_{s_j}$, and $x_{b_{2j}} = x_{s_{2j}}$, thus obtaining from (20)

$$\Lambda_j(\mathbf{r}; \mathbf{Y}) \sim \mathrm{Re}\,\frac{i\alpha^*\beta^*}{2v_o\bar{\zeta}}\sqrt{Q_{11}(z_{b_j})Q_{22}(z_{b_j})} \times \overset{+}{\delta}{}^{(3)}\left[-\frac{i}{2}T - v_o^{-1}\left(-2s\cos\bar{\vartheta}_{s_j} + \frac{Q_{11}}{2} \times (x_{s_{1j}}\cos\bar{\vartheta}_{s_j} \mp s\sin\bar{\vartheta}_{s_j})^2 + \frac{Q_{22}}{2}x_{s_{2j}}^2\right)\right]. \tag{21}$$

where $Q_{ii}(z_{b_j})$ are the elements of $\mathbf{Q}_j$ in [1, eq. (45)]. Inserting (21) into (19) and evaluating the integral in closed form we obtain (see Appendix)

$$\Gamma_j(s; \mathbf{Y}) \approx \frac{\pm\pi v_o^3}{8\cos 2\bar{\vartheta}_{s_j}\cos^4\bar{\vartheta}_{s_j}}\mathrm{Re}\left\{i\alpha^*\beta^*\overset{+}{\delta}{}^{(2)}(s)\right\}. \tag{22}$$

Next we note from [1, eq. (39)] that for real s, $\overset{+}{\delta}(s) = \delta(s) + i\mathcal{H}_s$, where $\mathcal{H}_s$ is a Hilbert transform with respect to s as discussed in [1, eq. (5)]. Substituting into (18), we obtain an expression that involves both the function $O_c(s)$ and its Hilbert transform. An expression that involves O_c alone is obtained if $i\alpha^*\beta^*$ is *real*. Since $\beta_r > 0$ while β_i may have any value, including zero (see guidelines for choosing β in Section III-B), we conclude that $\alpha_i \neq 0$ while α_r is determined via

$$\alpha_r = \alpha_i\beta_i/\beta_r. \tag{23}$$

With this choice, (18) simplifies to

$$U_j(\mathbf{Y}) = f(\bar{t}) \overset{\bar{t}}{\otimes} \frac{\pm\pi v_o^3}{\cos 2\bar{\vartheta}_{s_j}\cos^4\bar{\vartheta}_{s_j}}\frac{\alpha_i|\beta|^2}{8\beta_r}\partial_s^2 O_c(s; \mathbf{Y})|_{s=0}. \tag{24}$$

Equation (24) becomes more transparent if we consider a given $\mathbf{X} = (\bar{\mathbf{x}}, \bar{\boldsymbol{\xi}})$, which defines the PB axis and view $U_j(\mathbf{Y})$ as a function of $\bar{t}$. Thus, noting from (17) that $\partial s/\partial z_b = \cos\bar{\vartheta}_{s_j}$, (24) can be written as

$$U_j(\bar{t}) = f(\bar{t}) \overset{\bar{t}}{\otimes} \frac{\pm\pi v_o^3}{8\cos 2\bar{\vartheta}_{s_j}\cos^6\bar{\vartheta}_{s_j}}\frac{\alpha_i|\beta|^2}{\beta_r}\partial_{z_b}^2 O(\mathbf{r}_o(\mathbf{Y})). \tag{25}$$

where the sampling window center $\mathbf{r}_o(\mathbf{Y})$ is resolved by the time parameter $\bar{t}$ along the beam axis defined by $\mathbf{X}$ [see (16)].

Equation (25) provides a simple and direct relation between the local spectrum and the medium properties along the corresponding beam axis and may, therefore, be inverted. Noting from (16) that along the window center $dz_b/d\bar{t} = -v_o/(2\cos^2\bar{\vartheta}_{s_j})$, we obtain

$$O[\mathbf{r}_o(\mathbf{Y}(\bar{t}))] = \frac{\pm 2\beta_r \cos^2\bar{\vartheta}_{s_j}\cos 2\bar{\vartheta}_{s_j}}{v_o\pi\alpha_i|\beta|^2}\,\partial_{\bar{t}}^{-2} f^{\dagger}(\bar{t}) \overset{\bar{t}}{\otimes} U_j(\mathbf{Y}) \tag{26}$$

where $\partial_{\bar{t}}^{-1} \equiv \int_{-\infty}^{\bar{t}} d\bar{t}'$. The convolution with $f^{\dagger}(\bar{t})$ defined in (12), deconvolves the incident pulse $f(t)$ from the data and can be omitted for short-pulse excitation [see discussion in connection with (13)].

1) Axial and Cross-Axial Resolution: The axial resolution of the local spectrum analysis is determined by the excitation pulse $f(t)$. From (17), a short pulse with pulse length T_o can resolve details of order Δ_s

$$\Delta_s = \frac{v_o T_o}{2\cos\bar{\vartheta}_{s_j}}. \tag{27}$$

Thus, the spectral resolution deteriorates as $\bar{\vartheta}_{s_j}$ increases from best resolution for U_1 with small $\bar{\boldsymbol{\xi}}$ ($\bar{\vartheta}_{s_j} \to 0$) to worst resolution for U_2 with small $\bar{\boldsymbol{\xi}}$ ($\bar{\vartheta}_{s_j} \to \pi/2$). A similar conclusion has been reached previously for transient plane wave analysis [5] and by using asymptotic ray theory [7]. The resolution is also affected by the processing window: in order not to hamper the axial resolution, it is required that the *window* pulse length T be shorter than the *excitation* pulse length T_o. The cross-axial resolution is then determined by the beam width of the backpropagators which, from [1, eq. (55)] with [1, eq. (51)] and [1, eq. (49)], is roughly given by

$$D \sim 2\sqrt{v_o T \beta_r}. \tag{28}$$

2) Special Case: Backscattered Field with $\bar{\boldsymbol{\xi}} = 0$: Equation (27) establishes the backscattered local spectrum with $\bar{\boldsymbol{\xi}} = 0$ as the optimal case for high-resolution reconstruction. This special case corresponds to a z-directed backpropagated PB, implying that the $\overset{\circ}{\boldsymbol{\kappa}}_1$ and the $\overline{\mathbf{s}}_1$ axes are parallel to the $-z$ axis and $\bar{\vartheta}_{s_1} = 0$. Since for a given $(\overline{\mathbf{x}}, \bar{t})$, the center $\mathbf{r}_o(\mathbf{Y})$ of the PB is at $(\mathbf{x}, z) = (\overline{\mathbf{x}}, \frac{1}{2}(v_o\bar{t} + z_1))$ [cf. (16)], (25) becomes

$$U_1(\overline{\mathbf{x}}, \bar{\boldsymbol{\xi}} = 0, \bar{t}) = f(\bar{t}) \overset{\bar{t}}{\otimes} \frac{\alpha_i|\beta|^2}{8\beta_r}\,\pi v_o^3 \partial_z^2 O(\mathbf{r})|_{(\mathbf{x}, z) = (\overline{\underset{\sim}{\mathbf{x}}}, 1/2(v_o\bar{t} + z_1)/2)}. \tag{29}$$

By inverting (29)

$$O(\mathbf{r}) = \frac{2\beta_r}{v_o\pi\alpha_i|\beta|^2}\,\partial_{\bar{t}}^{-2} U_j(\mathbf{Y})|_{(\overline{\mathbf{x}}, \bar{\boldsymbol{\xi}}, \bar{t}) = (\mathbf{x}, 0, v_o^{-1}(2z - z_1))} \tag{30}$$

which is a special case of (26). For simplicity, the convolution with $f^{\dagger}$ in (26) has been removed.

C. Verification of the Locally Plane-Stratified Model

Here we demonstrate that the axial relations in (24) and (29) may alternatively be obtained by *assuming* a plane stratified medium whose stratification axis is along the bisectional direction $\overset{\circ}{\mathbf{s}}_j$, with wave speed equal to the wave speed along the beam axis corresponding to $\mathbf{X}$. For simplicity we consider only the case of a normally reflected PB as in (29) which implies that the medium is plane stratified along the z axis, with $v_c(z) = v(\mathbf{r})|_{\mathbf{x} = \overline{\mathbf{x}}}$. The field satisfies the 1-D wave equation

$$\left[\partial_z^2 - \frac{1}{v_c^2(z)}\,\partial_t^2\right] u(z, t) = 0 \tag{31}$$

which can be expressed alternatively as in integral equation for the scattered field

$$u^s(z, t) = -v_o^{-2}\partial_t^2 \int dz' \int dt' O_c(z') u(z', t') G(z, t; z', t') \tag{32}$$

where $O_c(z) = (v_o^2/v_c^2(z)) - 1$ and the 1-D free-space Green's function is $G(z, t; z', t') = (v_o/2)H(t - t' - |z - z'|/v_o)$, $H(t)$ being the Heaviside function. The Born approximation for the reflected field $u_1(t)$ at z_1 is obtained by substituting $u(z, t) \simeq u^i(z, t) = f(t - z/v_o)$ into (32) giving after a straightforward calculation

$$u_1(t) = f(t) \otimes \frac{-v_o}{8}\,\partial_z O(z)|_{z = 1/2(v_o t + z_1)}. \tag{33}$$

Next we calculate the local spectrum using the window function w of [1, eq. (38)]. Substituting into (1) with $\bar{\boldsymbol{\xi}} = 0$ and noting that u_1 is independent of $\mathbf{x}$ we arrive at

$$U_1(\overline{\mathbf{x}}, \bar{\boldsymbol{\xi}} = 0, \bar{t}) = 2\pi \int dt u_1(t) \int_0^{\infty} \rho d\rho w(\rho, t - \bar{t}) \tag{34}$$

where $\rho = |\mathbf{x} - \overline{\mathbf{x}}|$ and, from [1, eq. (15)] and [1, eq. (38)], $w(\rho, t) = \mathrm{Re}\{\alpha \overset{+}{\delta}{}^{(2)}(t - iT/2 - i\rho^2/2v_o\beta)\}$. Evaluating the ρ integral in closed form we obtain

$$U_1(\overline{\mathbf{x}}, \bar{\boldsymbol{\xi}} = 0, \bar{t}) = \int dt u_1(t)\,\mathrm{Re}\left\{2\pi v_o i\alpha\beta\,\overset{+}{\delta}{}^{(1)}(t - \bar{t} - iT/2)\right\}. \tag{35}$$

Finally, using $i\alpha\beta$ real as in (24) and assuming that $T \to 0$ we obtain, by inserting (33) into (35), the final expression in (29).

V. Numerical Example

In this section, we present a numerical example which implements the forward and inverse phase-space scattering theories in this two-part study. For the forward modeling, the implementation is centered around the relation in [1, eq. (26), fig. 6] between the local spectrum of the time dependent data, $U_j(\mathbf{Y})$ and the local sampling of the object function $O(\mathbf{r})$. We shall compare the evaluations of $U_j(\mathbf{Y})$ performed via two alternative routes: 1) direct evaluation from the time-dependent scattered field via (1) and b) evaluation via the spatial sampling of $O(\mathbf{r})$ appearing on the right-hand side of [1, eq. (26)]. The inverse modeling implements the reconstruction of $O(\mathbf{r})$ via (26), utilizing the calculated forward data for $U_j(\mathbf{Y})$.

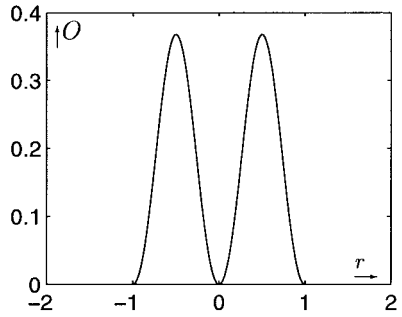

Fig. 3. Cross-sectional cut through the spherically symmetric function $O(\mathbf{r})$ used in the example.

A. Physical Configuration

We consider a three-dimensional (3-D) spherically symmetric inhomogeneous object confined within the sphere $r < 1$, where $r \equiv |\mathbf{r}|$. The radial dependence of $O(\mathbf{r})$ is given by

$$O(\mathbf{r}) = e^{-1} - (2r-1)^2 e^{-(2r-1)^2}, \qquad r < 1. \tag{36}$$

A cross section of O is depicted in Fig. 3. Note that the medium is continuous at the boundary $r = 1$. The background is assumed to be uniform with wave speed $v_o = 1$. The origin of coordinates is located at the center of the sphere, and scattered field data is taken on the measurement plane at $z = -2$. The incident pulse is the Gaussian

$$f(t) = T_0^{-1}\pi^{-1/2} e^{-(t/T_0)^2} \longleftrightarrow \hat{f}(\omega) = e^{-(T_0\omega/2)^2} \tag{37}$$

with the pulse length T_0 chosen to be 0.01, i.e., short on the object scale.

B. Evaluation of Scattered Field

The Born-approximated scattered field has been evaluated directly in the TD via [1, eq. (20)], which for the sake of numerical evaluation will be recast in the form

$$u_1(\mathbf{r}, t) = f^{(2)}(t) \overset{t}{\otimes} \frac{-1}{v_o^2} \int d^3r' \int dt' O(\mathbf{r}') \cdot u_\delta^i(\mathbf{r}', t') G(\mathbf{r}, t; \mathbf{r}', t'))|_{\mathbf{r}\in z_1\text{plane}} \tag{38}$$

where $u_\delta^i(\mathbf{r}, t) = \delta(t - z/v_o)$ simulates an impulsive incident wave. Here $f^{(2)}(t)$ is the second derivative of $f(t)$ where the term to the right of the convolution is the twice integrated (with respect to t) impulse response, hereafter denoted by $u_\delta^{(-2)}(\mathbf{r}, t)$. Due to the spherical symmetry of O, the resulting field depends only on (ρ, t) where $\rho = \sqrt{x_1^2 + x_2^2}$. The impulsive behavior of the incident plane wave field u_δ^i and of G reduces the integral for $u_\delta^{(-2)}$ in (38) to the two-dimensional surface integration

$$u_1(\rho, t) = f''(t) \overset{t}{\otimes} \frac{-1}{2\pi v_o} \int_1^{-1} dx_1' \int_{-\sqrt{1-x_1'^2}}^{\sqrt{1-x_1'^2}} dx_2' \cdot O(\rho', z')/(R' + z' - z_1) \tag{39}$$

where $z' = \frac{1}{2}(v_o t + z_1) - \frac{1}{2}|\mathbf{x} - \mathbf{x}'|^2/(v_o t - z_1)$, $-\sqrt{1-\rho'^2} < z' < \sqrt{1-\rho'^2}$, and $R' = \sqrt{|\mathbf{x} - \mathbf{x}'|^2 + (z' - z_1)^2}$. Next, the convolution of $u_\delta^{(-2)}$ with $f^{(2)}(t)$ is performed numerically. Since the Gaussian pulse width was taken to be short on the scale of the integrated data, the convolution yields essentially the second derivative of $u_\delta^{(-2)}$. The Gaussian pulse response and the twice-integrated impulse response $u_\delta^{(-2)}$ are shown in Figs. 4 and 5, respectively.

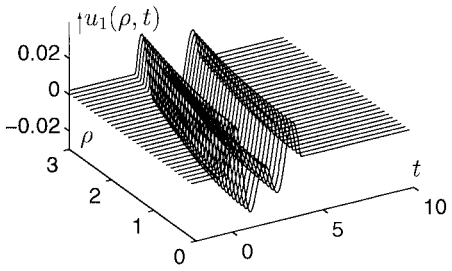

Fig. 4. Gaussian pulse response $u_1(\rho, t)$ under the Born approximation, evaluated at the $z_1 = -2$ plane.

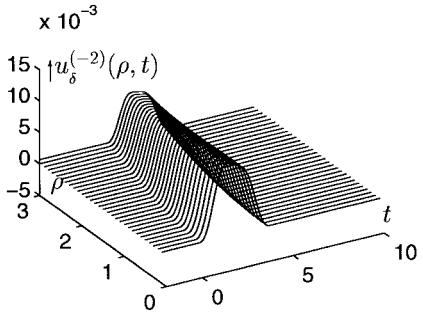

Fig. 5. Twice-integrated impulse response $u_\delta^{(-2)}(\rho, t)$ corresponding to the data in Fig. 4.

C. Calculation of the Local Spectrum

1) Calculation from the Data Via (1): We evaluate the local spectrum of the field in Fig. 4 for $\mathbf{X} = (\overline{\mathbf{x}}, \overline{\boldsymbol{\xi}}) = (0, 0)$, i.e., for a PB propagating along the z axis. Because of the problem symmetry, the 3-D [i.e., $(\mathbf{x}, t)$] integration in (1) reduces to a two-dimensional integral

$$U_1(\overline{t})|_{\mathbf{X}=(0,0)} = \int_0^\infty 2\pi\rho d\rho \int dt u_1(\rho, t) w(\rho, t - \overline{t}) \tag{40}$$

where $w(\rho, t)$ is the space–time processing window function in [1, eq. (38)], which for $\mathbf{X} = (0, 0)$, is given after (34). The window parameters chosen are $\beta = 5$, $\alpha = 1$ and $T = 0.01$ [T was chosen to be equal to the excitation pulse T_o of (37)]. Different sampling rates were tested. Convergence was achieved for temporal sampling at a rate of $\Delta_t = T/8$ which ensures a minimum of eight sampling points per window pulse length (see discussion following [1, eq. (42)]) and for spatial sampling at the rate of $\Delta_\rho = 0.025 = D/18$ [1, eq. (43)] which corresponds to 18 samples per window width D. The integration domain was restricted to $\rho < \rho_{\max} = 10D$ and $t_{\max} = 60T$ for which the integral converges. These results are in accord with a previous study on the numerical implementation of the local spectrum [4].

The resulting local spectrum $U_1(\overline{t})|_{\mathbf{X}=(0,0)}$ is shown in Fig. 6 (dashed curve). Note that this waveform exists mainly in the range $\overline{t} = [0, 4]$ corresponding to the axial data in Fig. 4. The slight broadening of the local spectrum with respect to

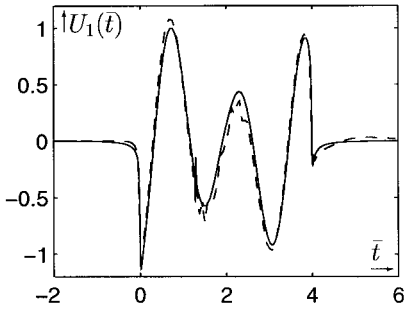

Fig. 6. Numerical results for the local spectrum U_1 as a function of $\bar{t}$ for $\bar{\mathbf{x}} = 0, \bar{\boldsymbol{\xi}} = 0$. Dashed curve: direct evaluation by processing the time-dependent data via (40). Solid curve: evaluation via spatial sampling of $O(\mathbf{r})$ via (41). Window parameters: $\beta = 5$, $\alpha = 1$, and $T = 0.01$.

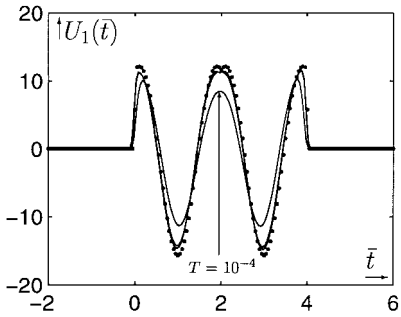

Fig. 7. The beam-axis approximation for the local spectrum $U_1(\mathbf{Y})$, calculated via (19) as a function of $\bar{t}$ for $\bar{\mathbf{x}} = 0, \bar{\boldsymbol{\xi}} = 0$ (dotted). This result is compared to $U_1(\mathbf{Y})$ as obtained by processing the data via (40) with three values of T: $T = 10^{-4}$, 10^{-5}, and 10^{-6} (full curves). Window parameters: $\beta = 5$ and $\alpha = -i$.

the range $\bar{t} = [0, 4]$ is attributed to the temporal width of the window.

2) Calculation by Object Space Sampling Via [1, eq. (26)]: To explain the results of the local spectrum, as calculated above by processing the scattered data, we calculate the local spectrum of the data from the local (phase-space) diffraction tomography relation in [1, eq. (26)], i.e., by local sampling of $O(\mathbf{r})$. The spatial window $\Lambda_1(\mathbf{r}'; \mathbf{Y})$ in [1, eq. (26)] corresponding to the data window $w(\mathbf{x}, t)$ in [1, eq. (38)] is given in [1, eq. (56)] with $\alpha = 1$. Setting $(\bar{\mathbf{x}}, \bar{\boldsymbol{\xi}}) = (0, 0)$, the object domain integration in [1, eq. (26)] is thus reduced to

$$U_1(\bar{t})|_{\mathbf{X}=(0,0)} = 2\pi \int_0^1 \rho' d\rho' \int dz' O(r') \Lambda_1(\rho', z'; \bar{t}) \qquad r' = \sqrt{\rho'^2 + z'^2} \tag{41}$$

with

$$\Lambda_1(\rho', z'; \bar{t}) \sim \mathrm{Re}\, \frac{i\beta^*}{2v_o} Q(z') \overset{+}{\delta}{}^{(3)} \left[\bar{t} - \frac{i}{2} T - v_o^{-1} \left(2z' - z_1 + \frac{1}{2} Q(z') \rho'^2 \right) \right] \tag{42}$$

where $Q(z') = (z' - z_1 - i\beta^*)^{-1}$. The resulting $U_1(\bar{t})$ is plotted in Fig. 6 (solid curve) on the same scale as the calculation of $U_1(\bar{t})$ via (40). The two waveforms are almost identical. This calibrates both the asymptotics so that [1, eq. (26)] with [1, eq. (56)] is valid for $T < 0.01$, and the numerical algorithm for the data processing in (1).

3) Calculation Via Beam-Axis Approximation (18): Finally, we validate the beam-axis sampling approximation for $U_1(\mathbf{Y})$ in (18) by comparison with the local spectrum calculation by processing the data via (40). For the case $\mathbf{X} = (0, 0)$ considered here, (18) reduces to (29); the window parameters were taken to be $\beta = 5$ and $\alpha = -i$ in accord with the condition discussed after (22). The result of (29) is shown in Fig. 7 (dotted curve) together with the results of (41) for the same values of α and β, and for three values of T, $T = 10^{-4}$, 10^{-5}, and 10^{-6} (solid curves). One observes that as T becomes successively shorter with respect to the scale of O, the local spectrum converges toward the result in (29).

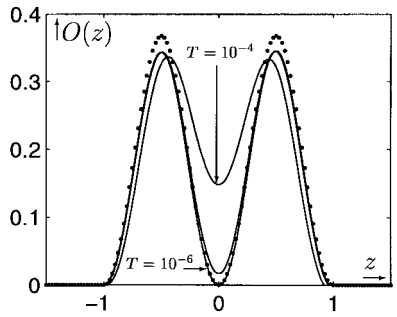

Fig. 8. Reconstruction along the beam axis. The three full curves are the results for $T = 10^{-4}$, 10^{-5}, and 10^{-6}. The dotted curve is the exact object function (36).

An analytic bound on the validity of the beam axis approximation can be found by expanding the object function $O(\mathbf{r})$ into a first-order Taylor series about the beam axis z

$$O(\rho, z) \simeq O(z) + O'(z) \frac{\rho^2}{2z} \tag{43}$$

where $\rho = \sqrt{x_1^2 + x_2^2}$ is the distance from the z axis. The beam axis approximation is valid if the second term in (43) may be neglected with respect to the first term for all $\rho < \rho_{\max}$ where $\rho_{\max}$ is the width of the transverse integration domain [see discussion after (40)]. Using (43) and (36) we obtain

$$\rho_{\max} \ll \sqrt{2zO(z)/|O'(z)|} \simeq 0.14. \tag{44}$$

Recalling that numerical convergence was obtained for $\rho_{\max} = 10D$, it follows using [1, eq. (43)] that T should satisfy $T \ll 10^{-5}$, which is in accord with the numerical results of Fig. 7.

D. Object Reconstruction

Finally, we use (30) to reconstruct the object function along the beam axis (which, for the present case of $\bar{\mathbf{x}} = 0, \bar{\boldsymbol{\xi}} = 0$, is simply the z axis). By applying (30) to the local spectrum shown in Fig. 7 for $T = 10^{-4}$, 10^{-5}, and 10^{-6}, we obtain three reconstructions of the object function. The results in

Fig. 8 (solid curves) demonstrate that good reconstruction is obtained for $T < 10^{-5}$.

VI. Concluding Remarks and Future Directions

In this two-part investigation, we have injected into the previously formulated plane-wave-based TD slant-stack diffraction tomography [5] the spatial resolution that results from PB postprocessing of the *scattered* field. By this mechanism, both the forward and inverse algorithms simplify substantially because the interrogated portion of the scattering domain is thereby localized to a space–time-resolved scattering cell. This cell orients itself dynamically with respect to the directions of incidence and observation in such a manner that it is replaced by an equivalent one-dimensionally stratified medium. A corresponding scattering phenomenology in terms of Fermat ray paths has been suggested as a better parameterizer of the highly localized wave physics. This trend is carried to its ultimate potential by PB preprocessing of the incident signal together with PB postprocessing of the scattered signal. Under these conditions, the scattering mechanism involves localized source domains and localized observation domains, which render the point-to-point Fermat ray paths as *the* logical model. The PB preprocessing is implemented via interrogation with a PB field [8]

$$u^i(\mathbf{r},\, t) = \frac{-i\beta^i}{z_i - i\beta^i}\, \overset{+}{\delta}\!\left[t - i\,\frac{1}{2}\,T_o - v_o^{-1} \cdot \left(z_i + \frac{1}{2}\,\rho_i^2/(z_i - i\beta^i)\right)\right] \tag{45}$$

where z_i and $\rho_i = \sqrt{x_{i_1}^2 + x_{i_2}^2}$ are the beam coordinates of the incident field obtained via a conventional rotation transform from $\mathbf{r}$ to $\mathbf{r}_i$ in the direction (ϑ_i, φ_i), which determines the incident beam axis. This incident PB gives rise to the Born-approximated induced sources which generate the scattered field. Applying the local transform and denoting by $U_j(\mathbf{Y}; \overset{\circ}{\boldsymbol{\kappa}}{}^i)$ the local spectrum on the z_j plane due to PB illumination in the direction $\overset{\circ}{\boldsymbol{\kappa}}{}^i$, we obtain

$$U_j(\mathbf{Y}; \overset{\circ}{\boldsymbol{\kappa}}{}^i) = \int d^3r' O(\mathbf{r}') \Lambda_j(\mathbf{r}';\, \mathbf{Y},\, \overset{\circ}{\boldsymbol{\kappa}}{}^i) \tag{46}$$

where the sampling window kernel is given by

$$\Lambda_j(\mathbf{r}';\, \mathbf{Y},\, \overset{\circ}{\boldsymbol{\kappa}}{}^i) = \int dt' u^i(\mathbf{r}',\, t';\, \overset{\circ}{\boldsymbol{\kappa}}{}^i)(-v_o^{-2})\partial_{t'}^2 \Psi_j(\mathbf{r}',\, t';\, \mathbf{Y}). \tag{47}$$

Here, Ψ_j is the wave object defined in [1, eq. (25)]. For the Gaussian δ window in [1, eq. (38)], this wave object is evaluated in [1, eq. (47)]. Thus, Ψ_j is a PB propagating in the direction $\overset{\circ}{\boldsymbol{\kappa}}_j$ determined by the phase-space (processing) variable $\overline{\boldsymbol{\xi}}$ via [1, eq. (17)]. $\mathbf{Q}_j$ and the beam coordinates are defined in [1, eq. (45)] and [1, eq. (46)]. Inserting [1, eq. (47)] into (46) we obtain

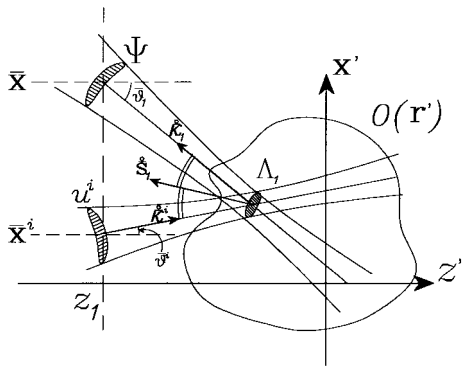

Fig. 9. (Time-domain local spectrum)—(object) relation under PB excitation. The figure depicts the incident PB u^i propagating in the $\overset{\circ}{\boldsymbol{\kappa}}{}^i$ direction and a scattered PB $B(\mathbf{r},\, t;\, \mathbf{Y})$ in the $\overset{\circ}{\boldsymbol{\kappa}}_1$ direction. This scattered PB is related via (46) to the local Radon transform of O over the spatial window $\Lambda_1(\mathbf{r}';\, \mathbf{Y})$. The scattering cell is oriented along the bisector $\overset{\circ}{\mathbf{s}}_1$ between $\overset{\circ}{\boldsymbol{\kappa}}{}^i$ and $\overset{\circ}{\boldsymbol{\kappa}}_1$.

$$\begin{aligned}\Lambda_j(\mathbf{r}';\, \mathbf{Y},\, \overset{\circ}{\boldsymbol{\kappa}}{}^i) &\sim \mathrm{Re}\,\frac{-1}{2v_o\overline{\zeta}}\,\frac{-i\beta^i}{z_i - i\beta^i}\,\sqrt{\frac{\det\,\mathbf{Q}_j(z_b')}{\det\,\mathbf{Q}_j(0)}} \\ &\quad \times \overset{t}{\delta}{}^{(3)}\!\left[\overline{t} - \frac{i}{2}\,(T + T_o) - v_o^{-1} \cdot \left(z_i' - z_b' + \frac{1}{2}\,(\rho_i'^2/(z_i - i\beta^i) + \mathbf{x}_b' \cdot \mathbf{Q}_j \cdot \mathbf{x}_b'\right)\right].\end{aligned} \tag{48}$$

This result implies the following. The sampling window in (48) is more localized *a priori* than the one in [1, eq. (56)] because any deviation ρ_i and/or $\mathbf{x}_b$ from its center coordinates gives rise to a complex delay and therefore to spatial damping with respect to the peak value $\rho_i = \mathbf{x}_b = 0$ on the incident beam axis. Since the window center is located along the incident PB axis, the phase-space variable $\mathbf{Y}$ should be chosen so as to ensure probing of the object function in the vicinity of this axis (see Fig. 9). The orientation of Λ_j can be found as in [1], but now it bisects the angle between $\overset{\circ}{\boldsymbol{\kappa}}{}^i$ and $\overset{\circ}{\boldsymbol{\kappa}}_1$, with $\overset{\circ}{\boldsymbol{\kappa}}{}^i$ beam steering allowing arbitrary look angles at the equivalent 1-D profile stratification. Another important advantage of the PB illumination is that it probes only the region relevant for imaging and thus minimizes scattering contributions from irrelevant zones.

It is now widely recognized that efficient and robust modeling of wave interaction with complex environments is aided substantially through the availability of phenomenology-matched efficiently calculable Green's functions, which furnish the building blocks for representation of arbitrary fields. The utility of such Green's functions is enhanced further if they also account for preprocessing and postprocessing options at their most elemental level. Within these perspectives, the PB scattering algorithm in (46)–(48) can be regarded as a phase-space Green's function for weak scattering scenarios that incorporates both the configurational (space–time) and the spectral (wavenumber-frequency) characteristics in the form

of analytic delta functions. Via analytic delta functions, which model physical wavepackets rather than spherical impulses, issues pertaining to resolution and related aspects are already taken into account.

The very preliminary numerical results presented here illustrate some of the forward and inverse modeling capabilities and efficiencies of the PB algorithm. These results look encouraging. Further studies will have to establish how this ultimately localized diffraction tomographic procedure compares with more conventional tomographic and other forward and inverse scattering techniques.

APPENDIX
DERIVATION OF (22)

Substituting (21) into (19) and changing variable to $y \equiv (x_{s_1} \mp s \tan \overline{\vartheta}_{s_j})$ we obtain

$$\Gamma_j(s) \simeq \mathrm{Re}\, \frac{-v_o \alpha^* \beta^* \partial_s^2}{8\pi \overline{\zeta} \cos^2 \overline{\vartheta}_{s_j}} \int dy h(y) \tag{49}$$

where

$$h(y) = \int dx_{s_2} \sqrt{Q_{11} Q_{22}} [c + a x_{s_2}^2]^{-2} \tag{50}$$

with $a = -Q_{22}/2v_o$ and $c = -(i/2)T - v_o^{-1}(-2 \cos \overline{\vartheta}_{s_j} s + \frac{1}{2} y^2 Q_{11} \cos^2 \overline{\vartheta}_{s_j} y^2)$. Next, using the standard integral $\int_{-\infty}^{\infty} (c + az^2)^{-2} dz = \pi (2a^{1/2} c^{3/2})^{-1}$, $\mathrm{Im}\sqrt{c/a} > 0$ we evaluate (50) as

$$h(y) = 2\pi v_o^2 \sqrt{Q}_{11} (i v_o T - 4 s \cos \overline{\vartheta} s + Q_{11} \cos^2 \overline{\vartheta}_{s_j} y^2)^{-3/2}. \tag{51}$$

To evaluate the y integral, we insert this result into (49) and neglect the y dependence of Q_{11}. Using $\int_{-\infty}^{\infty} (az^2 + c)^{-3/2} dz = 2(\sqrt{a} c)^{-1}$, $\mathrm{Re}\sqrt{c/a} > 0$ we obtain from (49) (recall that $\overline{\zeta} = \pm \cos 2\overline{\vartheta}_{s_j}$)

$$\Gamma_j(s) = \frac{\pm \pi v_o^3}{8 \cos 2\overline{\vartheta}_{s_j} \cos^4 \overline{\vartheta}_{s_j}} \partial_s^2 \cdot \mathrm{Re}\left\{ i \alpha^* \beta^* \overset{+}{\delta} [s - i v_o T/4 \cos \overline{\vartheta}_{s_j}] \right\}. \tag{52}$$

The width of this axial sampling window is given essentially by $v_o T/4 \cos \overline{\vartheta}_{s_j}$. Since $v_o T$ is small on the scale of O, the $-i v_o T/\cos \overline{\vartheta}_{s_j}$ term in (52) may be neglected, giving the result in (22).

REFERENCES

[1] T. Melamed, E. Heyman, and L. B. Felsen, "Local spectral analysis of short-pulse-excited scattering from weakly inhomogenous media—Part I: Forward scattering," *IEEE Trans. Antennas Propagat.*, this issue, pp. 1208–1217.

[2] T. Melamed and E. Heyman, "Spectral analysis of time-domain diffraction tomography," *Radio Sci.*, vol. 32, pp. 593–604, 1997.

[3] E. Heyman and L. B. Felsen, "Weakly dispersive spectral theory of transients (STT)—Part I: Formulation and interpretation; Part II: Evaluation of the spectral integral; Part III: Applications," *IEEE Trans. Antennas Propagat.*, vol. AP-35, pp. 80–86, Jan. 1987; pp. 574–580, May 1987; pp. 1258–1266, Nov. 1987.

[4] T. Melamed, "Phase-space beam summation: A local spectrum analysis for time-dependent radiation," *J. Electromagn. Waves Appl.*, vol. 11, pp. 739–773, 1997.

[5] T. Melamed, Y. Ehrlich, and E. Heyman, "Short-pulse inversion of inhomogeneous media: A time-domain diffraction tomography," *Inverse Problems*, vol. 12, pp. 977–993, 1996.

[6] T. Melamed, "Phase-space techniques for time-domain local inversion of inhomogeneous medium," Ph.D. dissertation, Tel-Aviv University, Israel, 1996.

[7] D. Miller, M. Orstaglio, and G. Beylkin, "A new slant on seismic imaging: Migration and integral geometry," *Geophys.*, vol. 52, pp. 943–964, 1987.

[8] E. Heyman, "Pulsed beam propagation in an inhomogeneous medium," *IEEE Trans. Antennas Propagat.*, vol. 42, pp. 311–319, Mar. 1994.

Timor Melamed, for a photograph and biography, see this issue, p. 1217.

Ehud Heyman (S'80–M'82–SM'88), for a photograph and biography, see p. 528 of the May 1995 issue of this TRANSACTIONS.

Leopold B. Felsen (S'47–A'53–M'54–SM'55–F'62–LF'90), photograph and biography not available at the time of publication.